J. Fluid Mech. (1995), vol. 291, pp. 343–368

The nonlinear evolution of magnetic instabilities in a rapidly rotating annulus

By KENNETH A. HUTCHESON AND DAVID R. FEARN

Department of Mathematics, University Gardens, University of Glasgow,
Glasgow G12 8QW, UK

(Received 9 June 1994 and in revised form 24 October 1995)

A numerical investigation of the stability of an axisymmetric magnetic field is discussed. The magnetic field permeates a finitely conducting fluid contained within a rapidly rotating cylindrical annulus. The fluid is incompressible and viscid. The evolution of a non-axisymmetric perturbation to the axisymmetric magnetic field is governed by the momentum and induction equations which are integrated using a spectral timestep method. We follow the growth of the perturbation to finite amplitude and find that the character of the solution is dominated by the most unstable axially dependent mode found from the linear theory.

1. Introduction and background

Evidence from the magnetization of ancient rocks has shown that, on average, the intensity of the Earth's magnetic field has remained relatively unchanged for the past 3 billion years. It is now generally accepted that this magnetic field is generated, and maintained, by fluid motion in the Earth's outer core where magnetic field lines of force are twisted and sheared by the flow, thus reinforcing the field. One of the most striking aspects of the Earth's magnetic field is that it reverses its sign every few hundred thousand years, although it only takes about ten thousand years for the field to reverse. The field also changes its configuration on shorter timescales. In particular a recent investigation of the magnetic field morphology at the Earth's core–mantle boundary (Bloxham, Gubbins & Jackson 1989) has shown that hydromagnetic wave-like oscillations have persisted for the past four hundred years. If such oscillations become large enough then they may cause the field pattern to change dramatically, and may trigger a reversal. Furthermore McFadden & Merrill (1993) carried out a statistical analysis of the reversal record and suggested a model whereby reversals of the field are triggered by internal instabilities of the fluid motion of the core. A study of the stability of the Earth's magnetic field may go some way to explain what fields are observed and how strong they are – the field is stable for long periods of geological time – and may lead to new ideas about reversal mechanisms. Extensive linear analyses of the stability of a toroidal magnetic field have been made. One of the simplest models is the field

$$\boldsymbol{B}_0 = B_M s F(s) \hat{\boldsymbol{\phi}}, \tag{1.1}$$

where (s^*, ϕ, z^*) are cylindrical polar coordinates, $s = s^*/s_o$, $z = z^*/s_o$, and B_M is a constant. This field permeates an electrically conducting fluid in a cylindrical annulus of outer radius s_o, and inner radius s_i, rotating rapidly about its axis with uniform angular velocity

$$\Omega_0 = \Omega_0 \hat{z}. \tag{1.2}$$

Field (1.1) is chosen as being representative of planetary magnetic fields since it is widely believed that strong toroidal fields are generated by shearing of poloidal magnetic field.

The linear stability of (1.1) has been investigated in a numerical study by Fearn (1983, 1984, 1985, 1988, 1989). Two types of instability have been found: ideal and resistive. The ideal mode was first discussed by Acheson (1972, 1973, 1978, 1983) who recognized that the instability is favoured by a strong gradient of the magnetic field (this instability is often referred to as the field gradient instability). Another distinguishing feature of this mode is that it can exist in the diffusionless (ideal) limit. The resistive mode requires some resonant surface $\boldsymbol{k} \cdot \boldsymbol{B}_0 = 0$ (where $\boldsymbol{k}$ is the wavenumber of the instability) and vanishes in the diffusionless limit – the resistive mode requires reconnection and breaking in the neighbourhood of the resonant surface.

A global condition for instability of field (1.1) was found, in terms of the Elsasser number, Λ, to be

$$\Lambda \geqslant \Lambda_c \geqslant O(1) \tag{1.3}$$

where

$$\Lambda = \tau_\eta / \tau_s, \quad \tau_\eta = s_o^2/\eta, \quad \tau_s = 2\Omega_0/\Omega_M^2, \tag{1.4}$$

and

$$\Omega_M = B_M / s_o(\mu \rho_o)^{1/2}. \tag{1.5}$$

The magnetic diffusivity η, magnetic permeability μ, and fluid density ρ_0 are all taken to be constant, Ω_M is the Alfvén frequency, τ_η is the ohmic decay time and τ_s is the 'slow' MHD timescale which is the natural timescale when there is a balance between Coriolis and Lorentz forces. The Elsasser number, Λ which may be written as the ratio between the Lorentz force and the Coriolis force (and is thought to be $O(1\text{–}100)$ for the Earth) can also be regarded as an inverse measure of magnetic diffusion. Fearn's (1983) model has been investigated further by Fearn & Weiglhofer (1992*a*) and extended to a spherical geometry by Fearn & Weiglhofer (1991*a*,*b*, 1992*b*) and more recently by Zhang & Fearn (1993, 1994).

These linear analyses have been important in advancing our knowledge of the conditions under which planetary magnetic fields become unstable but to examine how magnetic field instabilities evolve by extracting energy from the basic state requires a nonlinear analysis. To proceed we take a step backward and choose a cylindrical geometry instead of the more realistic spherical geometry. This choice simplifies the numerical approach substantially whilst retaining the essential physics of the problem.

An important aspect of the evolution of the instability is the concomitant evolution of the basic state. In the linear analysis it is sufficient to consider the basic state (for example (1.1)) as given and perform a stability analysis about the basic state. In the nonlinear problem, the basic state is an integral part of the solution since it is modified by the evolution of the instability and magnetic diffusion (this is also true for the linear problem, but in that case the solution may be thought of as an instantaneous snapshot). As a first approximation we consider the basic state as an ambient field that satisfies the relevant boundary conditions, and we assume that its diffusion is balanced by a dynamo generation not modelled here. However, we do calculate the perturbation to the basic state as the instability evolves. Ideally we

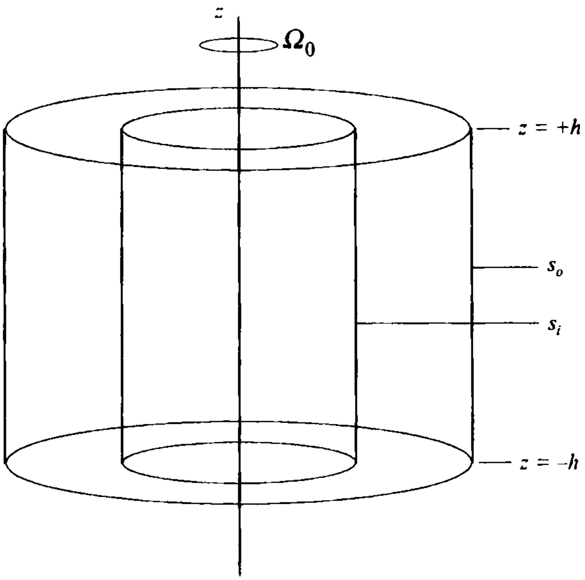

FIGURE 1. Geometry of the annular core model. The annulus is rotating rapidly about its axis, with uniform angular velocity $\Omega_0\hat{z}$.

would like to consider the basic state simply as an initial condition for the nonlinear problem, but the current approximation is a reasonable starting point for future calculations.

Another important consideration is the parameterization of the viscosity of the fluid in the Earth's core. The magnetostrophic approximation takes advantage of the fact that the viscosity is small by assuming that the dimensionless measure of the fluid viscosity, the Ekman number, $\epsilon = \nu/2\Omega_0 s_o^2$, is zero (where ν is the kinematic viscosity). However, Taylor (1963) showed that solutions can only exist if the magnetic field satisfies the constraint

$$\int_{C(s)} (\boldsymbol{J} \times \boldsymbol{B})_\phi \mathrm{d}\phi \mathrm{d}z = 0 \quad \forall s, \tag{1.6}$$

where $\boldsymbol{J}$ is the current density and $C(s)$ is the cylinder coaxial with the rotation axis, of radius s and contained within the core. This condition is modified if viscous boundary-layer effects are included. We therefore have a choice. We can either retain the Ekman number as a variable parameter of the problem, and choose a value that is small enough to be numerically tractable whilst being of geophysical interest, or we can choose to neglect the viscous effects in the main body of the fluid and deal with the problem of satisfying the modified Taylor integral separately. In this paper we choose the former approach, and retain ϵ as a free parameter.

The remainder of this paper is organized as follows. In §2 we describe our cylindrical model and write down the equations that govern the system. In §3 the numerical method (which is dealt with in an appendix) is tested against some well-known linear results. The nonlinear evolution of the instability and modified basic state are described in §4, and finally the results are discussed in §5.

2. A model of the Earth's core

The model we are investigating consists of a finite cylindrical annulus of inner radius s_i, outer radius s_o and height $2h$ which is rotating about its axis with angular velocity $\Omega_0 = \Omega_0\hat{\boldsymbol{z}}$. The region $\{s_i < s^* < s_o;\ \ -h < z^* < +h\}$ is filled with an incompressible conducting fluid of constant kinematic viscosity ν, magnetic diffusivity η, magnetic permeability μ, and density ρ_0. The regions $\{0 \leqslant s^* \leqslant s_i;\ \ -h \leqslant z^* \leqslant +h\}$ and $\{s_o \leqslant s^*;\ \ -h < z^* < +h\}$ are rigid and may be either perfect electrical insulators or perfect conductors. The regions $\{+h \leqslant z^*\}$ and $\{-h \geqslant z^*\}$ are perfect conductors and the boundaries at $z = \pm h$ are stress-free. The fluid moves with a velocity $\tilde{\boldsymbol{U}}^*$ and is permeated by a magnetic field $\tilde{\boldsymbol{B}}^*$. The model is shown in figure 1.

In a frame of reference co-rotating with the fluid the equations that govern the fluid motion and the evolution of the magnetic field are

$$\rho_o\left(\frac{\partial \tilde{\boldsymbol{U}}^*}{\partial t} + \tilde{\boldsymbol{U}}^*\cdot\nabla\tilde{\boldsymbol{U}}^* + 2\boldsymbol{\Omega}_0\times\tilde{\boldsymbol{U}}^*\right) = -\nabla\tilde{P}^* + \mu^{-1}(\nabla\times\tilde{\boldsymbol{B}}^*)\times\tilde{\boldsymbol{B}}^* + \rho_o\nu\nabla^2\tilde{\boldsymbol{U}}^*, \quad (2.1)$$

$$\frac{\partial \tilde{\boldsymbol{B}}^*}{\partial t} = \nabla\times(\tilde{\boldsymbol{U}}^*\times\tilde{\boldsymbol{B}}^*) + \eta\nabla^2\tilde{\boldsymbol{B}}^*, \quad (2.2)$$

$$\nabla\cdot\tilde{\boldsymbol{U}}^* = \nabla\cdot\tilde{\boldsymbol{B}}^* = 0, \quad (2.3)$$

where $\tilde{P}^*$ is the fluid pressure. Since we are only interested in magnetic instabilities, buoyancy effects are not included and we do not solve a corresponding forcing equation. By introducing a non-dimensionalization based on length s_o, time τ_s, and magnetic field strength B_M, (2.1)–(2.3) may be written as

$$\Lambda\epsilon_\eta\left[\frac{\partial \tilde{\boldsymbol{U}}}{\partial t} + \tilde{\boldsymbol{U}}\cdot\nabla\tilde{\boldsymbol{U}}\right] + \hat{\boldsymbol{z}}\times\tilde{\boldsymbol{U}} = -\nabla\tilde{P} + (\nabla\times\tilde{\boldsymbol{B}})\times\tilde{\boldsymbol{B}} + \epsilon\nabla^2\tilde{\boldsymbol{U}}, \quad (2.4)$$

$$\frac{\partial \tilde{\boldsymbol{B}}}{\partial t} = \nabla\times(\tilde{\boldsymbol{U}}\times\tilde{\boldsymbol{B}}) + \Lambda^{-1}\nabla^2\tilde{\boldsymbol{B}}, \quad (2.5)$$

$$\nabla\cdot\tilde{\boldsymbol{U}} = \nabla\cdot\tilde{\boldsymbol{B}} = 0, \quad (2.6)$$

where the magnetic Ekman number and the Ekman number, are defined by

$$\epsilon_\eta = \eta/2\Omega_0 s_o^2, \qquad \epsilon = \nu/2\Omega_0 s_o^2. \quad (2.7)$$

The Elsasser number, Λ and the slow MHD timescale, τ_s are defined in §1. In the following analysis we set the magnetic Ekman number ϵ_η to zero since the dynamo timescale is very much longer than the rotation period, Ω_0^{-1}. As a consequence, the character of the momentum equation changes from prognostic to diagnostic. Using this non-dimensionalization the height of the cylinder is 2ζ where $\zeta = h/s_o$. Also we do not define a measure of the velocity field strength: the scale of the velocity is defined implicitly by s_o and τ_s.

Since we want to examine how a non-axisymmetric instability evolves by extracting energy from an axisymmetric field it is useful to separate $\tilde{\boldsymbol{B}}$, $\tilde{\boldsymbol{U}}$ and $\tilde{P}$ into axisymmetric and non-axisymmetric components

$$\tilde{\boldsymbol{U}} = \boldsymbol{U}(s,z,t) + \boldsymbol{u}(s,\phi,z,t);\ \ \langle\boldsymbol{u}\rangle = 0, \quad (2.8)$$

$$\tilde{\boldsymbol{B}} = \boldsymbol{B}(s,z,t) + \boldsymbol{b}(s,\phi,z,t);\ \ \boldsymbol{B}(s,z,t) = \boldsymbol{B}_0(s) + \delta\boldsymbol{B}(s,z,t);\ \ \langle\boldsymbol{b}\rangle = 0, \quad (2.9)$$

$$\tilde{P} = P(s,z,t) + p(s,\phi,z,t),\ \ \langle p\rangle = 0, \quad (2.10)$$

where $\boldsymbol{B}_0(s)$ is the ambient basic state and $\delta\boldsymbol{B}$ is the axisymmetric perturbation from the basic state and

$$\langle f(s,\phi,z)\rangle = \frac{1}{2\pi}\int_0^{2\pi} f(s,\phi,z)\mathrm{d}\phi$$

where f is either p or any of the components of $\boldsymbol{u}$ or $\boldsymbol{b}$. Moreover, we carry out a poloidal–toroidal decomposition of the magnetic and velocity fields

$$\boldsymbol{U} = W\hat{\boldsymbol{\phi}} + \boldsymbol{U}_P, \qquad \boldsymbol{U}_P = \nabla\times V\hat{\boldsymbol{\phi}}, \qquad \boldsymbol{u} = \nabla\times v\boldsymbol{s} + \nabla\times\nabla\times w\boldsymbol{s}, \tag{2.11}$$

$$\boldsymbol{B} = (G_0 + \delta G)\hat{\boldsymbol{\phi}} + \boldsymbol{B}_P, \qquad \boldsymbol{B}_P = \nabla\times H\hat{\boldsymbol{\phi}}, \qquad \boldsymbol{b} = \nabla\times h\boldsymbol{s} + \nabla\times\nabla\times g\boldsymbol{s}. \tag{2.12}$$

Similar decompositions for the non-axisymmetric fields were used by Jones (1985). The solenoidal and incompressibility conditions (2.6) are automatically satisfied by (2.11) and (2.12) and the number of dependent variables is kept to a minimum – a feature that is important in the numerical solution of (2.4)–(2.6) (see the Appendix). Substituting (2.8)–(2.12) into (2.4)–(2.6), the separated equations can be written as

$$-\frac{\partial V}{\partial z} - \epsilon \mathrm{D}^2 W = [(\nabla\times\boldsymbol{B})\times\boldsymbol{B}]_\phi + \langle(\nabla\times\boldsymbol{b})\times\boldsymbol{b}\rangle_\phi, \tag{2.13}$$

$$-\frac{\partial W}{\partial z} + \epsilon(\mathrm{D}^2)^2 V = [\nabla\times((\nabla\times\boldsymbol{B})\times\boldsymbol{B})]_\phi + \langle\nabla\times((\nabla\times\boldsymbol{b})\times\boldsymbol{b})\rangle_\phi, \tag{2.14}$$

$$\frac{\partial(\delta G)}{\partial t} - \Lambda^{-1}\mathrm{D}^2(\delta G) = [\nabla\times(\boldsymbol{U}\times\boldsymbol{B})]_\phi + (\nabla\times\langle\boldsymbol{u}\times\boldsymbol{b}\rangle)_\phi, \tag{2.15}$$

$$\frac{\partial H}{\partial t} - \Lambda^{-1}\mathrm{D}^2 H = (\boldsymbol{U}\times\boldsymbol{B})_\phi + \langle\boldsymbol{u}\times\boldsymbol{b}\rangle_\phi, \tag{2.16}$$

$$\begin{aligned}\hat{\boldsymbol{z}}\times\boldsymbol{u} = -\nabla p &+ ((\nabla\times\boldsymbol{B})\times\boldsymbol{b} + (\nabla\times\boldsymbol{b})\times\boldsymbol{B}) \\ &+ \epsilon\nabla^2\boldsymbol{u} + [(\nabla\times\boldsymbol{b})\times\boldsymbol{b} - \langle(\nabla\times\boldsymbol{b})\times\boldsymbol{b}\rangle],\end{aligned} \tag{2.17}$$

$$\begin{aligned}\frac{\partial\boldsymbol{b}}{\partial t} = \nabla\times(\boldsymbol{u}\times\boldsymbol{B}) &+ \nabla\times(\boldsymbol{U}\times\boldsymbol{b}) + \Lambda^{-1}\nabla^2\boldsymbol{b} \\ &+ [\nabla\times(\boldsymbol{u}\times\boldsymbol{b}) - \langle\nabla\times(\boldsymbol{u}\times\boldsymbol{b})\rangle],\end{aligned} \tag{2.18}$$

where

$$\mathrm{D}^2 = \left(\nabla^2 - s^{-2}\right).$$

Equations (2.13)–(2.16) govern axisymmetric field evolution and (2.17) and (2.18) govern non-axisymmetric field evolution. The final diagnostic non-axisymmetric equations are found from $\boldsymbol{s}\cdot\nabla\times(2.17)$ and $\boldsymbol{s}\cdot\nabla\times\nabla\times(2.17)$. As a consequence the fluid pressure is eliminated from the equations. Similarly, the prognostic non-axisymmetric induction equations are found from $\boldsymbol{s}\cdot(2.18)$ and $\boldsymbol{s}\cdot\nabla\times(2.18)$.

By choosing stress-free and perfectly conducting flat ends at $z = \pm\zeta$ the boundary conditions on total fields $\tilde{\boldsymbol{U}}$ and $\tilde{\boldsymbol{B}}$ are

$$\hat{\boldsymbol{z}}\cdot\tilde{\boldsymbol{U}} = \tilde{\boldsymbol{S}}_{iz}\hat{\boldsymbol{z}} = 0, \tag{2.19}$$

and

$$\hat{\boldsymbol{z}}\cdot\tilde{\boldsymbol{B}} = \hat{\boldsymbol{z}}\times\tilde{\boldsymbol{E}} = 0, \tag{2.20}$$

where $\tilde{\boldsymbol{E}}$ is the total electric field and $\tilde{\boldsymbol{S}}_{iz}$ is the rate-of-strain tensor – i is either s or ϕ (see, for example, Gubbins & Roberts 1987). This choice has been made for numerical convenience and enables us to readily expand the dependent variables in terms of complete sets of functions in z that automatically satisfy the boundary conditions – see the Appendix. Once the ϕ-dependence has been expanded using Fourier series, we are left with an order-20 system in the independent variable s. We therefore need 10 boundary conditions at each of the sidewalls to determine the integration constants. Given that the sidewalls are rigid the boundary condition on the velocity field $\tilde{\boldsymbol{U}}$ is simply

$$\tilde{\boldsymbol{U}} = 0. \tag{2.21}$$

Our condition on the magnetic field $\tilde{\boldsymbol{B}}$ is that the field matches some external potential field, Φ, such that

$$\tilde{\boldsymbol{B}}^{(e)} = -\nabla\Phi; \quad \nabla^2\Phi = 0. \tag{2.22}$$

Solutions to (2.13)–(2.18) with velocity boundary conditions (2.21) and magnetic boundary conditions (2.22), are found using a spectral method in space and a conditionally stable semi-implicit timestepping method in time. Details of the numerical method can be found in the Appendix.

3. Algorithm testing in the linear regime

Accurate tests of the spectral-timestep (ST) code were carried out by comparing our results with those found from the linear stability analysis of a basic state. In the linear problem the axisymmetric field is fixed, equations (2.13)–(2.16) do not participate and the bracketed terms in (2.17) and (2.18) (the nonlinear interaction of non-axisymmetric fields) can be ignored. It is a simple matter to remove the nonlinear contribution from the ST code and compare our results with results from linear eigenvalue (LE) codes.

Our main source of comparison is with the finite difference LE code of Fearn (1983) in which a single angular (ϕ, z) mode is chosen (i.e. the azimuthal wavenumber m and axial wavenumber n are chosen) and its destabilizing effect upon a basic state is investigated. In particular, the finitely conducting viscid region is divided into a finite number of steps, differential operators are replaced by fourth-order finite difference operators and the resulting banded matrix eigenvalue problem is solved using inverse iteration. The returned eigenvalue is the complex growth rate of the instability, λ. An approximation to λ can be readily found at time t from the ST code using a first-order Taylor expansion,

$$\lambda = \frac{1}{\Delta t}\left[\frac{v(t+\Delta t)}{v(t)} - 1\right] \quad \text{for } \Delta t \ll 1, \tag{3.1}$$

where v stands for any of the components of $\boldsymbol{u}$ or $\boldsymbol{b}$ and Δt is the timestep.

The first basic state we examined was the toroidal field of Fearn (1983)

$$\boldsymbol{B} = B_M sF(s)\hat{\boldsymbol{\phi}}; \qquad \text{where } F(s) = [2/(1-s_{ib}^{\alpha})]^2[1-s^{\alpha}][s^{\alpha}-s_{ib}^{\alpha}], \tag{3.2}$$

which is illustrated in figure 2 for $\alpha = 4.0$ ($s_{ib} = s_i/s_o$, and we choose $s_{ib} = 0.35$ in all the calculations in this paper). The smooth line represents the exact function $F(s)$, and the dots indicate the points in radius where our collocation equations (and boundary conditions) are solved for $L = 10$. Setting $m = 1, n = 3$ (where $n = k\pi/2\zeta$, see Appendix), $\alpha = 4, \epsilon = 10^{-5}$ and $U = 0$ and incorporating insulating boundaries, the LE code locates a mixed mode instability (i.e. a mode that does not behave completely like either of the categories of 'ideal' or 'resistive', see Fearn 1988) with $\Lambda_c \approx 16.8088$ and $\omega_c \approx -1.05027$ (the negative sign indicates westward propagation).

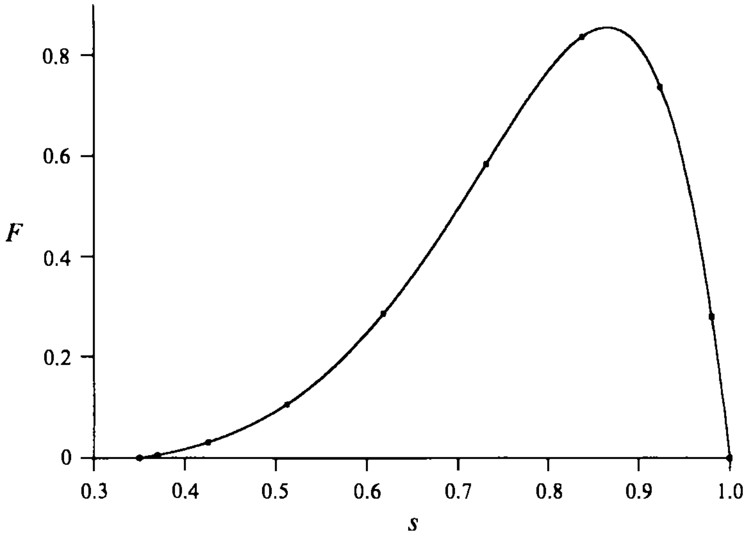

FIGURE 2. Field $F(s)$ given by (3.2) for $\alpha = 4.0$.

L	$\Delta t = 1\times10^{-3}$	$\Delta t = 5\times10^{-4}$	$\Delta t = 1\times10^{-4}$	$\Delta t = 5\times10^{-5}$
10	(−0.19462, −1.1333)	(−0.19527, −1.1339)	(−0.19579, −1.1343)	(−0.19585, −1.1343)
15	(−0.00094, −1.0490)	(−0.00134, −1.0496)	(−0.00166, −1.0502)	(−0.00170, −1.0502)
20	(0.00074, −1.0487)	(0.00034, −1.0494)	(0.00002, −1.0499)	(0.00002, −1.0500)
25	(0.00071, −1.0490)	(0.00003, −1.0496)	(−0.00001, −1.0502)	(−0.00005, −1.0502)
30	(0.00073, −1.0490)	(0.00033, −1.0496)	(0.00001, −1.0502)	(−0.00003, −1.0503)
35	(0.00073, −1.0490)	(0.00033, −1.0496)	(0.00002, −1.0518)	(−0.00003, −1.0502)

TABLE 1. λ found from ST code. (LE code: $\lambda = (0.370806 \times 10^{-4}, -1.0503)$.)

We ran our ST code with $A = 16.8088$, and kept all other parameters the same as in the LE code. Table 1 shows results for the critical growth rate, λ found from the ST code for various values of the timestep, Δt and at varying radial truncations, L. First, notice that an $L = 10$ truncation gives a poor approximation to λ for any practical value of Δt: we need at least $L = 15$ to resolve the thin boundary layers that develop for $\epsilon = 10^{-5}$. Using the critical frequency found from the LE calculation as our benchmark, the $L = 15, \Delta t = 10^{-3}$ solution is 99.88% accurate whereas the $L = 30, \Delta t = 5 \times 10^{-5}$ is 99.998% accurate. However, the trade-off in the required CPU time to achieve the slightly higher accuracy is large. The $L = 15, \Delta t = 10^{-3}$ calculation takes $\sim$ 87.5 CPU seconds for a time integration of $10\tau_s$ on a DEC-α. The corresponding $L = 30, \Delta t = 5 \times 10^{-5}$ calculation takes $\sim$ 5776 CPU seconds. By setting $m = 2, n = 3, \alpha = 1, \epsilon = 10^{-5}$, and $U = 0$, in the LE code a resistive mode with $\omega_c \approx 0.17187$ at $A_c \approx 29.29717$ was found for basic state (3.2). Setting $A = 29.29717, \Delta t = 10^{-3}, L = 35$, the ST code gave $\omega_c \approx 0.17176$.

In these checks we have set $U = 0$. To test the effect of the differential rotation in our ST code we temporarily introduce another dimensionless parameter, the modified magnetic Reynolds number, $\mathcal{R}_m$, defined by

$$\mathcal{R}_m = \frac{U_M \tau_s}{s_o} = \frac{R_m}{\Lambda}; \quad R_m = \frac{U_M s_o}{\eta}, \tag{3.3}$$

where U_M is a measure of the strength of the toroidal flow given by $U = U_M s \Omega(s) \hat{\boldsymbol{\phi}}$. With $m = 2, n = 3, \alpha = 4, \epsilon = 10^{-5}$ and $R_m = 10$ the LE code located the point of marginal stability at $\Lambda_c = 9.31994$ ($\mathcal{R}_m = 1.07297$) and $\omega_c = 0.453241$. The equivalent ST calculation with $L = 35, \Delta t = 10^{-3}$ gives $\omega_c = 0.4516812$ for $\Lambda = 9.31994$.

Finally, we looked at a mode that was ideal in character. Using a toroidal field as in (3.2) but with $F = s^\alpha$ and choosing the parameters $\Lambda = 90, m = 1, n = 2.1, \alpha = 1, \epsilon = 10^{-3}$ the LE code gives $\lambda = (0.4743441 \times 10^{-2}, -0.285199)$ – the corresponding ST calculation with $L = 14, \Delta t = 10^{-3}$ gives $\lambda = (0.47437318 \times 10^{-2}, -0.28600623)$. In summary, these tests have shown that the timestep code agrees well with the eigenvalue code, and it is clear from table 1 that we can achieve any desired degree of accuracy with an appropriate choice of L and Δt.

4. Equilibrated field solutions for moderate Ekman number

4.1. *Solutions at* $\Lambda = 12$

One of the main considerations in performing the nonlinear spectral calculations is computer time and storage, and as is usual in numerically intensive endeavour, there is a substantial trade-off between physical realism and obtainable results.

Our first concession is our choice of Ekman number, ϵ. It is well known that viscous boundary layers, which have thicknesses proportional to ϵ, develop near the boundaries of a contained, rapidly rotating fluid. In the Earth the viscosity is poorly determined, but it is generally agreed that its value is small. As discussed in the introduction we have chosen to retain ϵ as a variable parameter and in the first instance we attempt to solve the instability equations with the most practical and most realistic Ekman number. For this we have chosen $\epsilon = 10^{-3}$ for the remaining set of calculations. This is obviously a higher value than we would wish to use but it does mean that we do not have to resolve excessively narrow boundary layers, which, in turn means that we need fewer functions in our spectral expansions.

Our second concession regards the basic state. Here, we constrain the basic state, so that it may be considered to be an ambient state (see equation (2.15) where it is only the perturbation, δG, that is subject to diffusion). We can therefore regard the maintenance of the basic state as part of the dynamo problem which we are not considering here. In some ways this is similar to the investigation of kinematic dynamos where a fluid flow is imposed (for example an $\alpha\omega$-effect) and its forcing is not considered. The basic state we chose is given by (3.2) and is shown in figure 2. This field has the feature that it automatically satisfies the insulating boundary conditions (a field proportional to some power of the radius obviously cannot do so). This is an important consideration, because although we are constraining the system to always contain the basic state, we also solve the axisymmetric part of the problem, so we need a field that satisfies the boundary conditions. Our complete set of parameters is therefore

$$\epsilon = 10^{-3}; \ \alpha = 4.0; \ \zeta = \pi/2. \tag{4.1}$$

The first part of the analysis is to find the critical onset (i.e. find Λ_c) from the linear theory. We used a combination of the ST code and the LE code to determine

m	$n \approx 0$	$n=1$	$n=2$	$n=3$	$n=4$	$n=5$	$n=6$
1	9.43	10.46	19.76	31.86	45.90	61.75	78.91
2	10.02	10.59	16.47	32.00	66.36	133.51	234.15
3	16.24	18.39	27.69	56.12	165.90	1066.05	62796.1
4	34.55	39.59	60.24	125.20	379.96	1961.99	23920.7
5	89.29	101.97	152.88	306.87	855.56	3540.01	24402.3
6	264.12	299.50	438.47	838.27	2134.02	7461.83	37616.6

TABLE 2. $\Lambda_c(m,n)$ for $\epsilon = 10^{-3}; \alpha = 4$.

onset. The important feature here is to find Λ_c for the most unstable mode. For $\Lambda > \Lambda_c$ growing solutions exist. For parameter set (4.1) the most unstable mode is $(m = 1, n = 0)$ for which $\Lambda_c \approx 9.428$. A summary of $\Lambda_c(m,n)$ is shown in table 2.

For our first nonlinear ST calculation we chose a value of $\Lambda = 12 > \Lambda_c$ (note that at $\Lambda = 12$ the $(m = 1, n = 0)$ mode is not the fastest growing mode). Our ST parameters were $L = 10, K = 6$ (where K is the truncation in the z-direction – see Appendix), $M = 6, \Delta t = 5 \times 10^{-4}$. Henceforth we will refer to the L, K, M combination as (L, K, M). The initial conditions for the calculation were $\boldsymbol{B}$ given by (3.2), $\boldsymbol{U} = 0$ and a random small perturbation in each mode for $\boldsymbol{b}$ and $\boldsymbol{u}$ where the z-independent $(n = 0)$ modes were given smaller amplitudes relative to the other modes since they imply an infinite lengthscale in the z-direction. Equations (2.13)–(2.18) were then solved as discussed in the Appendix. Initially, the total fields $\tilde{\boldsymbol{B}}$ and $\tilde{\boldsymbol{U}}$ appeared to equilibrate fairly rapidly with the non-axisymmetric $(m = 2, n = 1); (m = 4, n = 0, 2)$ modes dominating the equilibration (see figure 3, $50\tau_s < t < 100\tau_s$). However a closer inspection of the fields showed that the $(m = 1, n = 1)$ mode was growing whilst the $(m = 2, n = 1)$ modes were decaying (see figure 3, $100\tau_s < t < 175\tau_s$). After timestepping further the solution reached a true equilibration (see figure 3, $t > 200\tau_s$). The final equilibrated solution has the following parity:

$$m \text{ and } n \text{ even} \quad \textit{or} \quad m \text{ and } n \text{ odd},$$

and consists of a steady axisymmetric part and a time-varying non-axisymmetric part. A number of different initial conditions were then implemented (including a set with large-amplitude z-independent terms) to check the integrity of our solution and in each case we found the final equilibrated solution to be the same.

In figure 4 we show the axisymmetric field components of the equilibrated field in the (s, z)-plane where we have taken the annulus and sliced it vertically through the z-axis. The sections are the right-hand elevations, the dotted lines represent flow or magnetic flux into the page and the solid lines represent flow or magnetic flux out of the page. The δB_ϕ component represents the deviation from the original ambient field. In general the axisymmetric field components have relatively smooth representations and are dominated by low-wavenumber (l, n) combinations. In particular, the U_s and U_z components are dominated by the $n = 2$ mode whereas the U_ϕ component has an $n = 2$ dependence near to the outer boundary and an $n = 0$ dependence (i.e. a uniform differential rotation) near the inner boundary. Notice also that the magnitude of the poloidal velocity field components is much smaller than the toroidal component. It is clear that no narrow viscous boundary layers are present. The axisymmetric velocity

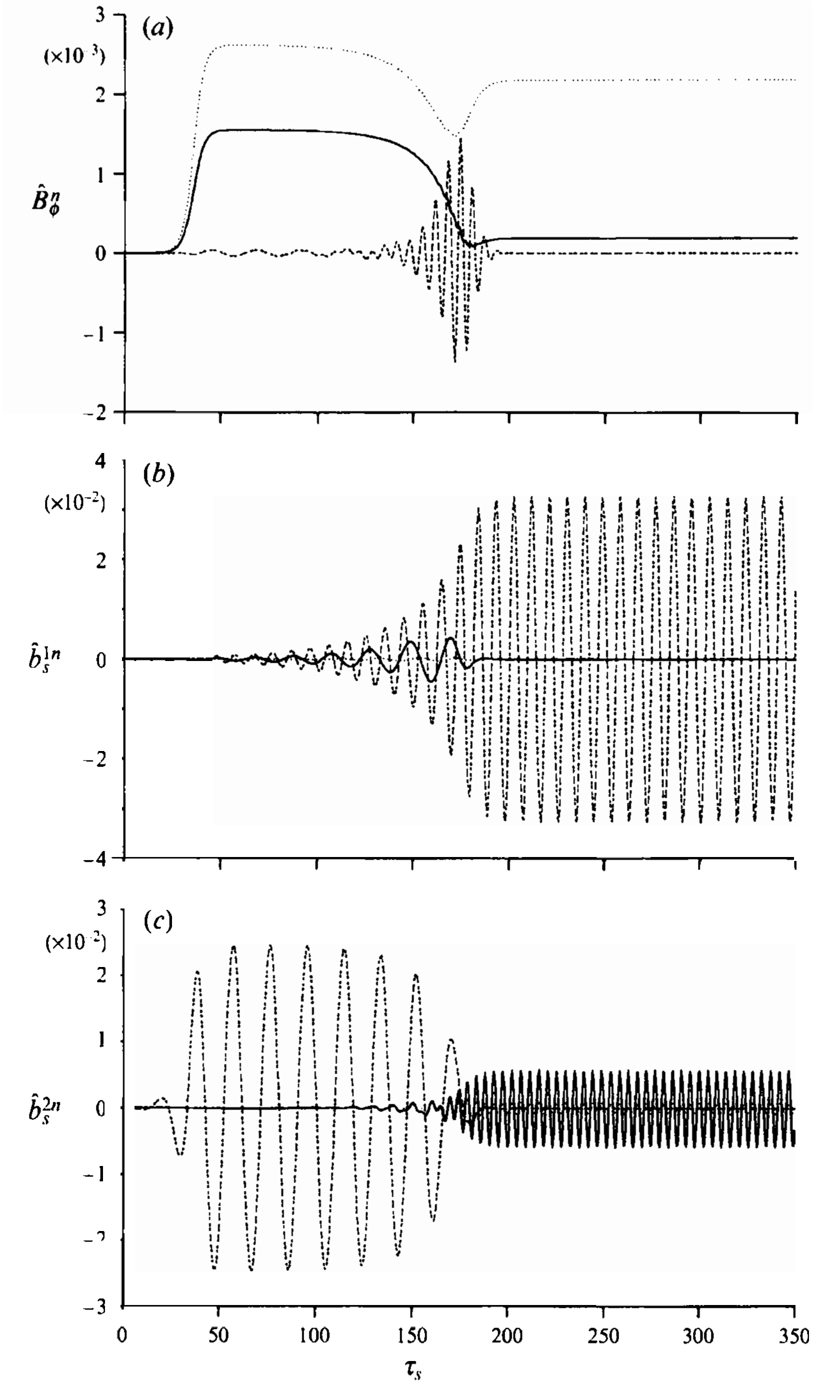

FIGURE 3 (*a,b,c*). For caption see facing page.

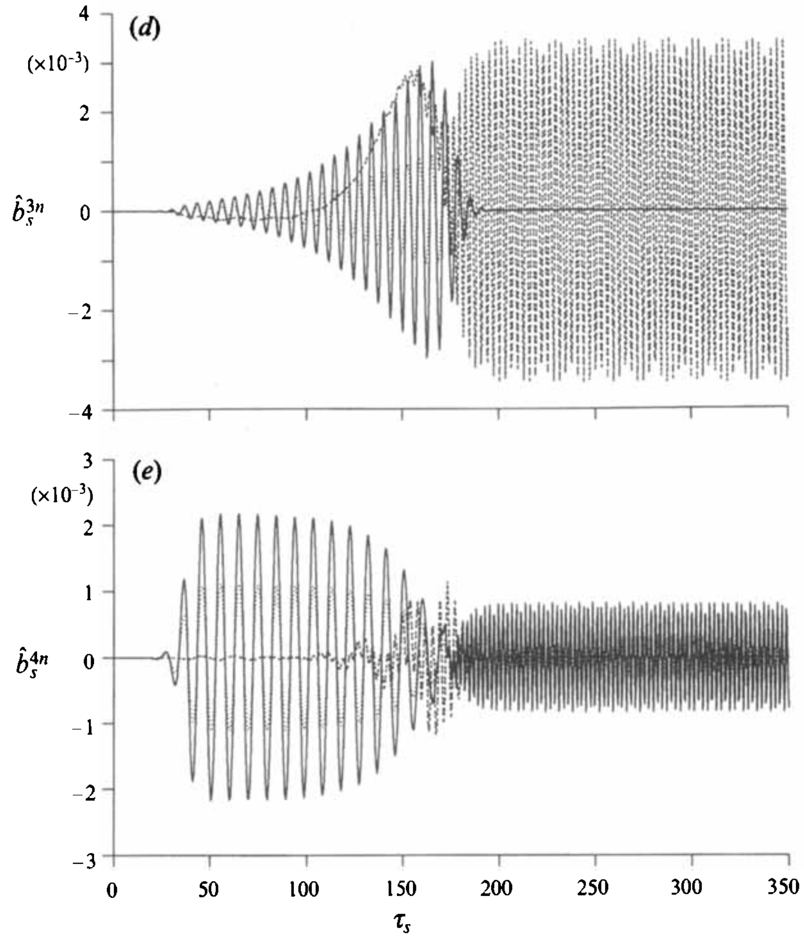

FIGURE 3. Amplitude of the low-order magnetic field modes in mixed physical–spectral space (x, n, m) plotted as a function of time: the solid line is $n = 0$, the dashed line is $n = 1$ and the dotted line is $n = 2$. (*a*) $\hat{B}_\phi$, (*b*) $\hat{b}_s(m = 1)$, (*c*) $\hat{b}_s(m = 2)$, (*d*) $\hat{b}_s(m = 3)$, (*e*) $\hat{b}_s(m = 4)$.

field has grown and equilibrated to its steady state through the action of the nonlinear Lorentz force – our initial conditions contained no axisymmetric velocity.

Recalling that the amplitude of the basic state $\tilde{\boldsymbol{B}}$ is $O(1)$, it is clear that the poloidal magnetic field components are considerably smaller in amplitude than the toroidal part, δB_ϕ. The poloidal field components, B_s and B_z, are dominated by an $n = 2$ structure. The axisymmetric magnetic and velocity field components exhibit definite symmetries about the plane $z = 0$: s- and ϕ-components are symmetric about $z = 0$ and z-components are antisymmetric about $z = 0$. The observed symmetry is due to symmetry of the problem under reflection about the midplane $z = 0$ (see, for example, Knobloch 1994).

In figure 5 the total radial field and total radial flow components for $\Lambda = 12$ are shown. Notice that we only plot the s, ϕ cross-section (at $z = +\zeta/4$) at one instant in time since the field patterns rotate rigidly in time. The most striking feature of the s, ϕ plot is the dominance of the $m = 1$ mode, and it turns out that this rotating wave propagates in a westwardly direction with a period of roughly ten slow timescales. Notice that despite the $m = 1$ dominance other modes have been excited which

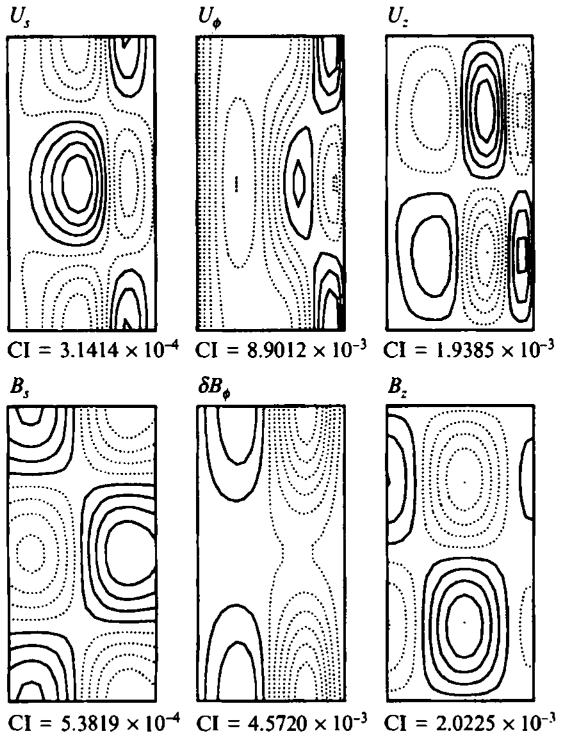

FIGURE 4. Steady axisymmetric field components of the equilibrated solution $\Lambda = 12$ in the (s, z)-plane, right elevation. CI is the dimensionless contour interval.

distorts the $m = 1$ picture slightly. It is also clear from the solution that the field and flow are, as expected, tied together and the flow anchors the field. Also shown in figure 5 is the temporal evolution of $\tilde{B}_s$ and $\tilde{U}_s$ in the sz-plane at $\phi = 0$. Notice the dominance of the axial wavenumber $n = 1$.

As discussed above, the linear theory predicts that the most unstable mode is the axially independent $m = 1$ mode, which has an infinite period. Here, the equilibrated nonlinear solution is, in fact, dominated by the $m = 1, n = 1$ mode, i.e. the most unstable axially dependent mode. For example the frequency, $\omega_{1,1}$, of the $m = 1, n = 1$ non-axisymmetric mode shown in figure 5 is -0.67389202 and the frequencies of the other modes that contribute to the final solution are related to the 'resonant' frequency by $\omega_{m,n} = m \times \omega_{1,1}$. Note that from the linear theory the critical frequency of $\omega_{1,1}$ is -0.66286501.

As in the linear spectral analysis the convergence in space and time of the final solution is important if we are to view the figures 4 and 5 with any confidence. We have checked the convergence of the final solution both qualitatively and quantitatively. We increased/decreased the truncation parameters (L, K, M) to find new solutions: if the new solutions at different truncation are substantially different then our solution has not converged to its true solution. As a quantitative check on convergence we calculated the total magnetic energy, E_M, (found by taking the scalar product of (2.5) with $\tilde{\boldsymbol{B}}$ and integrating over the volume of the annulus) for various truncations. The results are shown in table 3. It is clear that as the number of angular functions, T_a, is increased from 16 to 42 (keeping the radial truncation fixed at $L = 10$), E_M converges. Although the $m = 1, n = 1$ mode dominates the final solution we need several m and

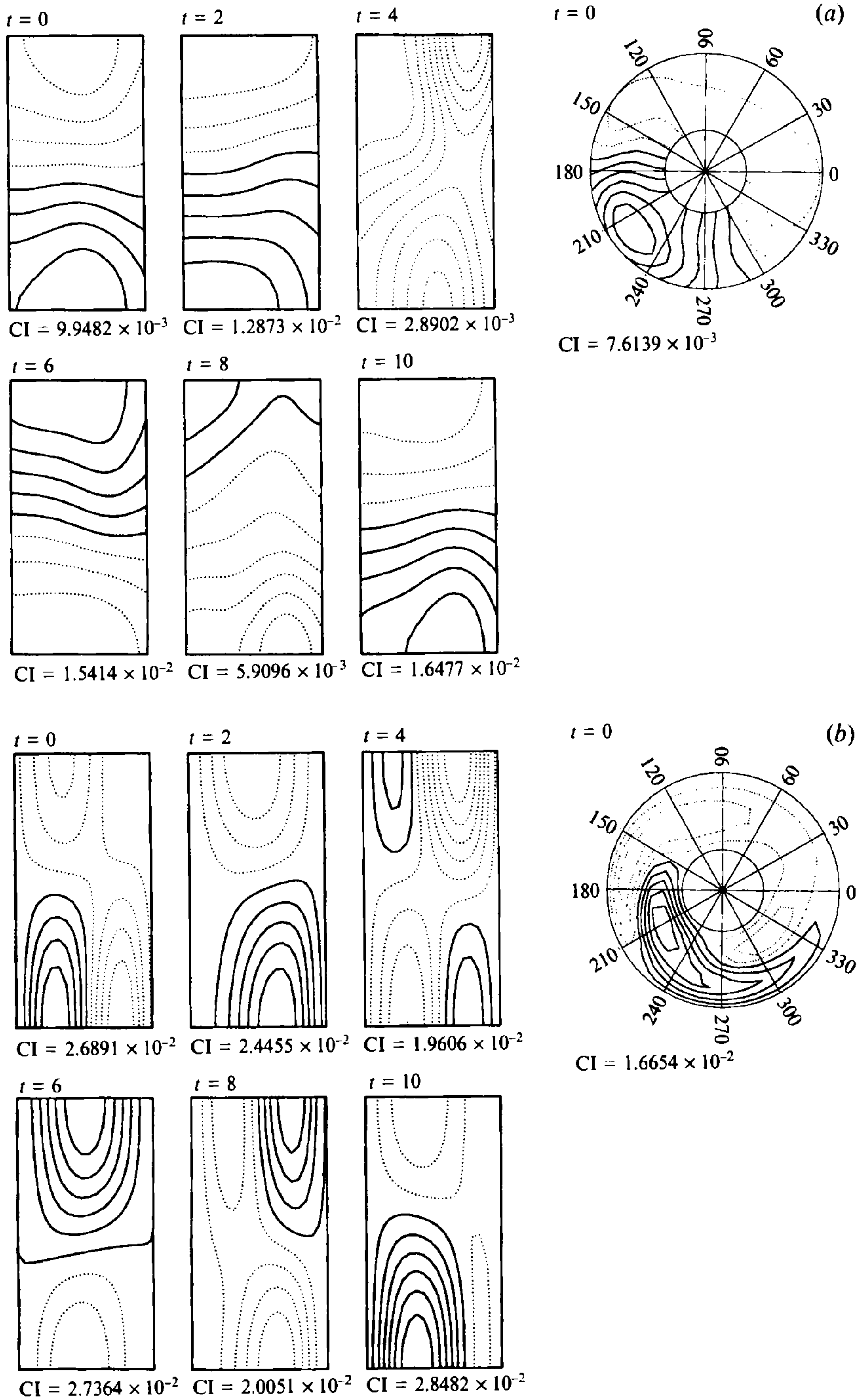

FIGURE 5. Evolution of total field components (a) $\tilde{B}_s$ and (b) $\tilde{U}_s$ plotted over 10 slow timescales in the (s, z)-plane at $\phi = 0$ and at $t = 0$ in the (s, ϕ)-plane at $z = \zeta/4$ for $\Lambda = 12$.

(L,K,M)	T_a	$E_M \times 10^{-2}$
(10, 3, 4)	16	9.3674
(10, 4, 4)	20	9.3627
(10, 4, 4)†	20	9.3546
(10, 4, 5)	25	9.4318
(10, 5, 5)	30	9.4315
(14, 6, 6)	42	9.1004
(19, 6, 6)	42	9.1026

TABLE 3. Convergence of E_M where T_a is the total number of angular modes. †ST calculation with $\Delta t = 2.5 \times 10^{-4}$.

n modes since energy is transferred from the low-order modes to the higher-order modes. As we increase the radial truncation L from 10 to 14 to 19, E_M also converges. Notice also that the reduction in timestep from $\Delta t = 5 \times 10^{-4}$ to $\Delta t = 2.5 \times 10^{-4}$ shows that the solution is also well converged in time. Qualitative convergence checks were made by comparing field plots for various truncations, and the differences between the plots for the truncations shown in table 3 are negligible. We are therefore confident that our (10, 6, 6) solution is representative of the converged solution, and continue with this truncation parameter set in the calculations below.

4.2. *Solutions at higher Λ*

Subsequently, we varied Λ systematically to see what effect this has on the solution. Calculations were carried out at $\Lambda = 14, 16, \ldots, 30$ where the 'previous' solution was used as the initial condition for the 'current' Λ. We have not calculated solutions for $\Lambda > 30$ since considerably more modes are excited and the truncation required becomes impractical. In figures 6 and 7 we plot field components for $\Lambda = 20$ and in figures 8 and 9 the fields are plotted for $\Lambda = 30$. Energy convergence checks were made at $\Lambda = 20$ and $\Lambda = 30$ for truncation parameter set (10,6,6) which showed that this set gives adequate spatial resolution. Figures 6 and 8 show that the axisymmetric fields retain their relatively smooth character although the field strengths increase as Λ is increased from $\Lambda = 20$ to $\Lambda = 30$. The toroidal field components have essentially the same structure as the field is increased and near the outer vertical boundary an $n = 4$ structure is evident for U_ϕ. There is a similar axially dependent structure for the B_s poloidal field component. These higher axial wavenumber features are not present in the $\Lambda = 12$ axisymmetric cross-section (see figure 4). In general, although the field components for $\Lambda = 20$ and $\Lambda = 30$ are similar, the structure of the field components for $\Lambda = 12$ is quite different, especially the radial structure of the poloidal components. For example, if the $\Lambda = 20$ and $\Lambda = 30$ U_z-components are compared with their $\Lambda = 12$ counterpart then it is clear that not only has the field increased in strength, but its structure has changed.

Figures 7 and 9 show the total radial field and flow components for $\Lambda = 20$ and $\Lambda = 30$ respectively. It is clear that the fields are no longer completely dominated by the $m = 1$ mode, and the emergence of an $m = 2$ feature can be seen as the field strength is increased. As in the $\Lambda = 12$ calculation the field and flow are tied and the field strength increases as Λ is increased. Also the waves propagate in a westwardly

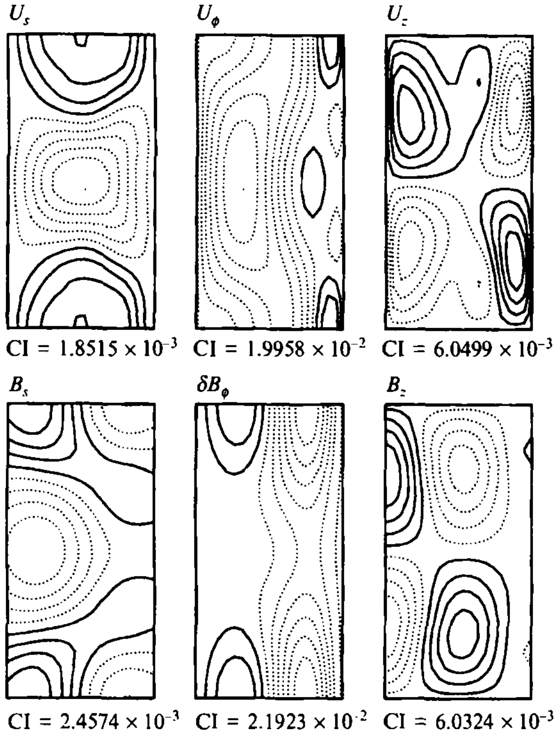

FIGURE 6. As figure 4 but $\Lambda = 20$.

direction and again the frequency of the solution is closely related to the frequency of the $(m = 1, n = 1)$ mode.

In figure 10 the amplitude of the non-axisymmetric field component b_s at a point in space $(s = 0.62, \phi = \pi/2, z = +\zeta/4)$ is plotted as a function of time for $\Lambda = 12, 20, 30$. As Λ is increased the local maximum that occurs between two global maxima becomes more pronounced – the spatial representation of this effect is the emergence of the $m = 2$ feature. Also, the mean ϕ-component of the Lorentz force $\langle \tilde{\boldsymbol{J}} \times \tilde{\boldsymbol{B}} \rangle_\phi$ is plotted in figure 11 for $\Lambda = 12, 20, 30$. Notice that much of the structure is concentrated near to the vertical boundaries and that its magnitude is small in the main body of the fluid. This is especially true for $\Lambda = 30$ (figure 11*c*).

The total magnetic energy E_M is plotted as a function of Λ in figure 12 (Λ_c is marked for reference). As Λ is increased above critical the system equilibrates to a finite-amplitude solution – the critical onset is as predicted by the linear theory and the amplitude of the solution near to critical is finite, but too small to be seen clearly on this graph. The trend shown in figure 12 is indicative of a supercritical bifurcation. No evidence of subcritical behaviour was found, i.e. no growing (stable or unstable) solutions were found for $\Lambda < \Lambda_c$, and in each subcritical search the fields decayed rapidly.

Figure 13 shows ξ plotted as a function of Λ, where

$$\xi = \frac{\displaystyle\int \left| \int \langle \tilde{\boldsymbol{J}} \times \tilde{\boldsymbol{B}} \rangle_\phi \mathrm{d}z \right| s^2 \mathrm{d}s}{\displaystyle\int\!\!\int |\langle \tilde{\boldsymbol{J}} \times \tilde{\boldsymbol{B}} \rangle_\phi| \mathrm{d}z s^2 \mathrm{d}s}. \tag{4.2}$$

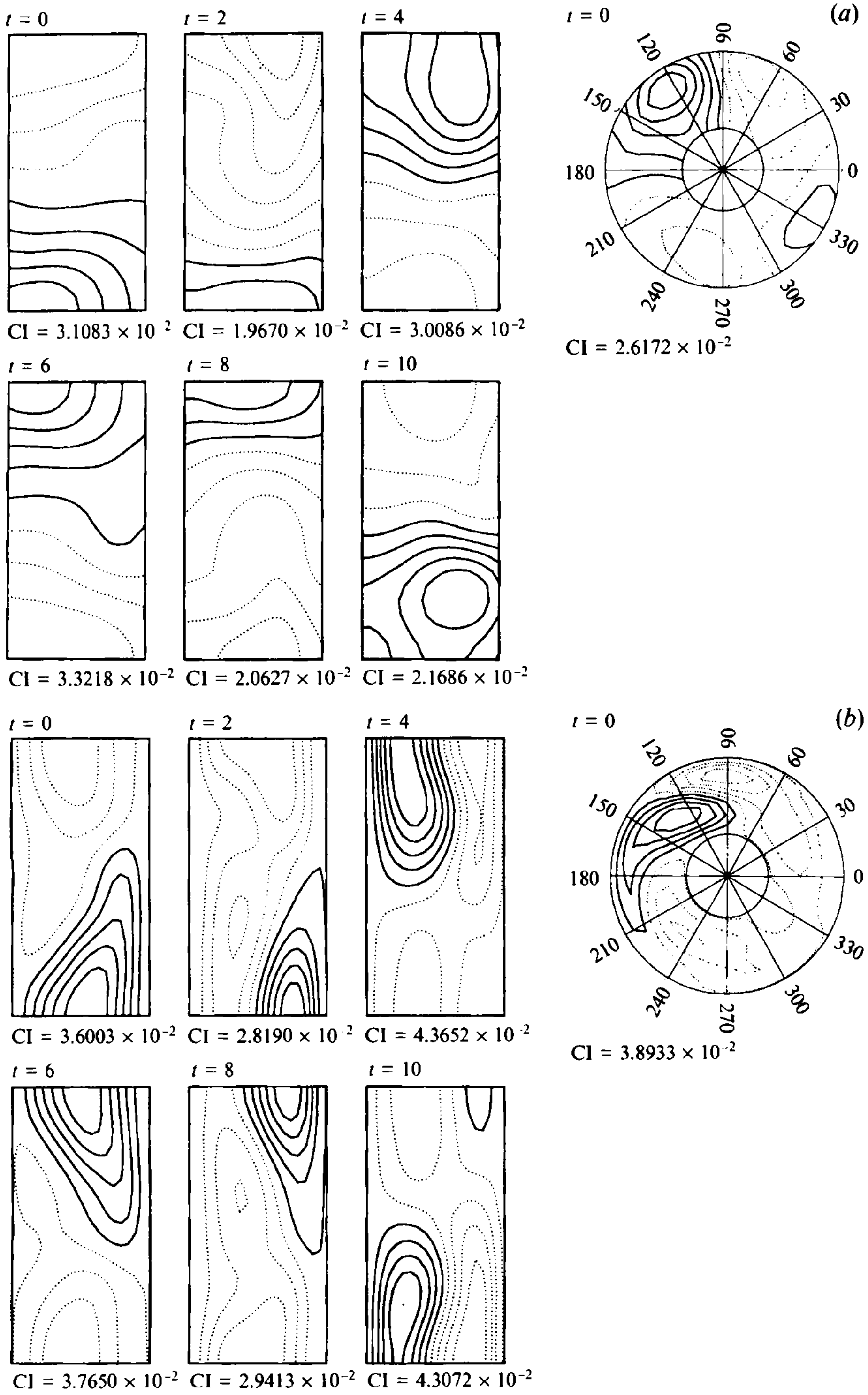

FIGURE 7. As figure 5 but $\Lambda = 20$.

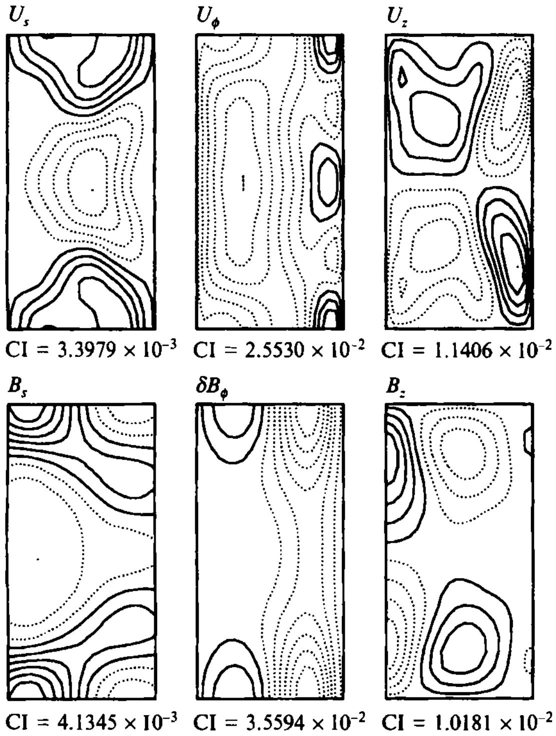

FIGURE 8. As figure 4 but $\Lambda = 30$.

ξ is a measure of the degree to which Taylor's constraint is satisfied (Ierley 1985). As Λ is increased through Λ_c, ξ increases to a maximum near $\Lambda = 20$ and then steadily decreases thereafter, i.e. the solution becomes less viscously limited as Λ is increased – recall that the structure of the axisymmetric ϕ-component of the Lorentz force was restricted to the boundaries as Λ was increased and that its amplitude became smaller in the main body of the fluid (figure 11). The best we can say from this is that the solutions we have found are of Ekman type (i.e. they are viscously limited) although the effects of viscosity become less pronounced as the field strengthens. For viscously limited solutions the magnetic field should scale as $\sim \epsilon^{1/2}$ (see, for example, Hollerbach & Ierley 1991). The maxima of $\tilde{B}_s$ for varying Λ, ψ_Λ, in the (s, ϕ)-plane at $z = +\zeta/4$, are $\psi_{12} \approx 0.025; \psi_{20} \approx 0.073; \psi_{30} \approx 0.072$ ($\epsilon^{1/2} \approx 0.0316$ for $\epsilon = 10^{-3}$) and the amplitude we find is not inconsistent with the $\epsilon^{1/2}$ scaling (future calculations at varying ϵ should verify this scaling). In contrast, for true Taylor-type solutions the magnetic field is $O(1)$ and the effects of viscosity are limited to narrow boundary layers, and can be neglected in the main body of the fluid.

In figure 14 the frequency of the $(m = 1, n = 1)$ mode is plotted as a function of Λ. The frequency of this mode for the linear and the nonlinear solutions is very similar, but has slightly smaller magnitude for the nonlinear solution as Λ is increased – this is due to the nonlinear mode interaction: the linear frequency is calculated in isolation and does not depend on the other modes. In the nonlinear case the frequency of the whole solution (as is evident in the s, ϕ plots) is characterized by the frequency of the $(m = 1, n = 1)$ mode despite energy transfer from this mode to higher $(m = 2, 3, \ldots)$ modes as Λ is increased.

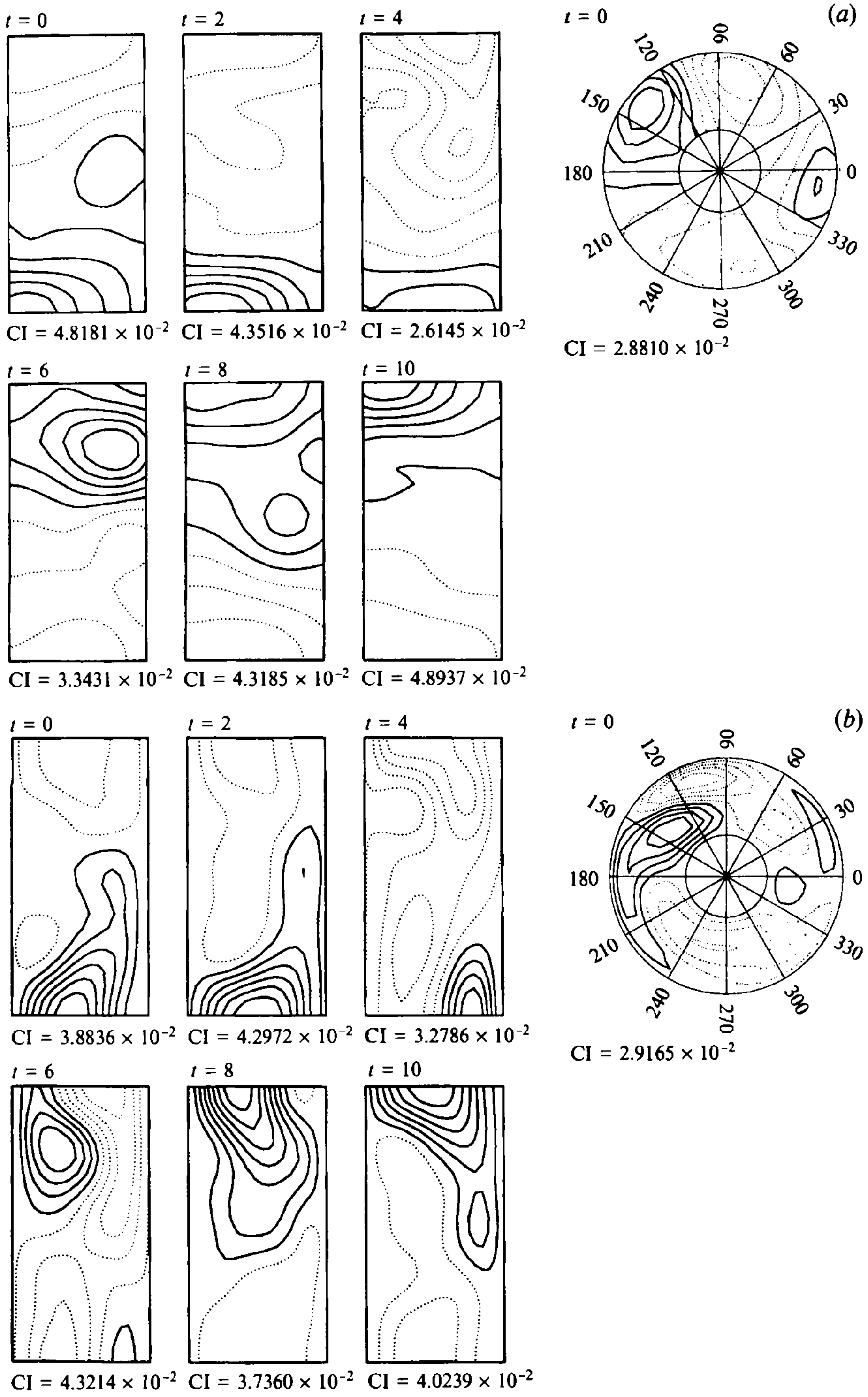

FIGURE 9. As figure 5 but $\Lambda = 30$.

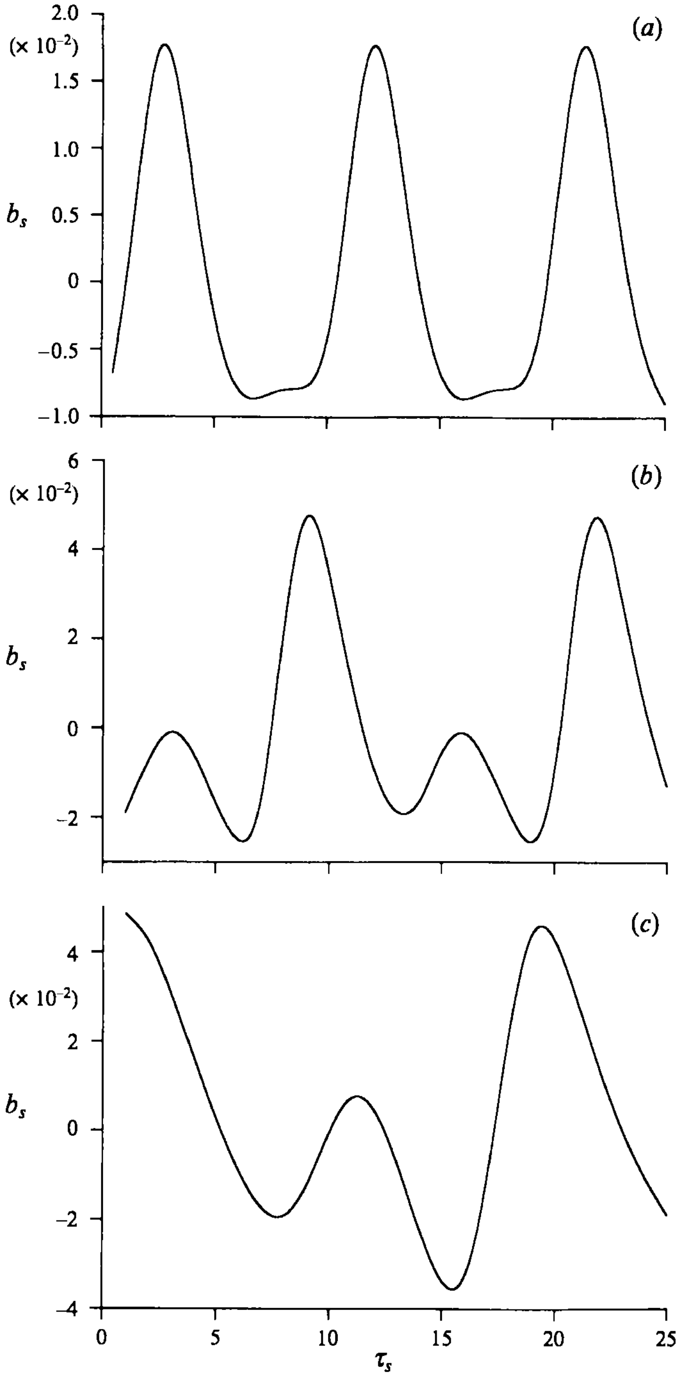

FIGURE 10. Amplitude of the non-axisymmetric field component b_s at $(s = 0.62, \phi = \pi/2, z = \zeta/4)$ plotted as a function of time for (*a*) $\Lambda = 12$, (*b*) $\Lambda = 20$, (*c*) $\Lambda = 30$.

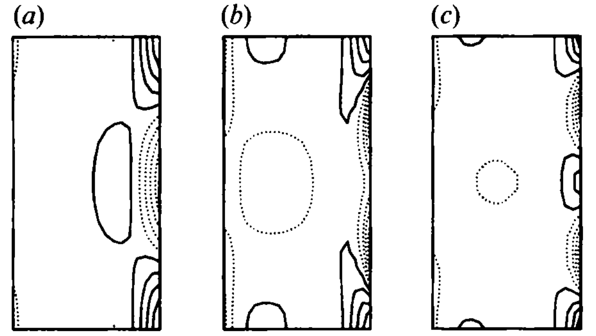

CI = 6.5022×10^{-3} CI = 1.2928×10^{-2} CI = 2.9836×10^{-2}

FIGURE 11. $\langle \tilde{\boldsymbol{J}} \times \tilde{\boldsymbol{B}} \rangle_\phi$ plotted in the (s,z)-plane for (a) $\Lambda = 12$, (b) $\Lambda = 20$, (c) $\Lambda = 30$.

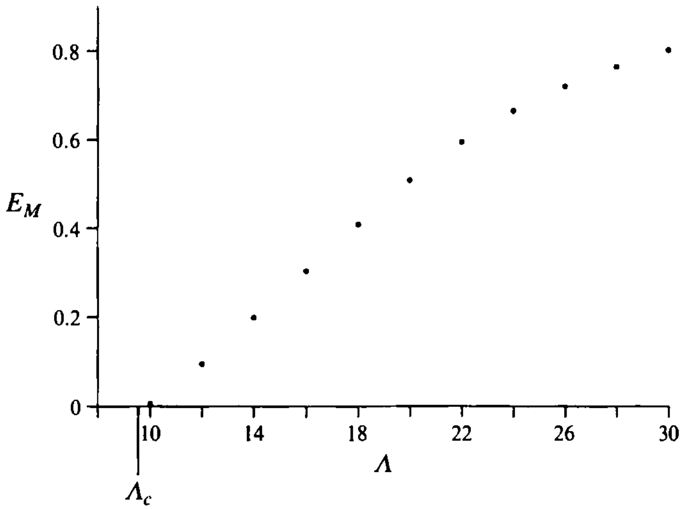

FIGURE 12. Total magnetic energy E_M plotted as a function of Λ. (Λ_c found from the linear analysis is marked for reference.)

5. Discussion

The above analysis has shown that above the critical onset predicted from the linear theory the solution equilibrates to finite amplitude on the stable branch of the energy bifurcation diagram. The equilibration mechanism is through nonlinear interaction (Lorentz force and advection) and is dominated by the most unstable axially dependent mode which determines the frequency of the whole solution – the nonlinear solution is 'trapped' by the dominant linear mode. Further, the equilibrated solutions exist in a state that has a finite axisymmetric differential rotation in the inner region of the annulus – a feature that generally tends to stabilize solutions in the linear regime.

Of particular interest is the critical nature of the bifurcation diagram shown in figure 12. Here we could only find supercritical solutions for our chosen basic state whereas subcritical solutions may be more representative of the type of instabilities that trigger magnetic field reversal – the field remains stable for long periods of geological time but reverses fairly rapidly.

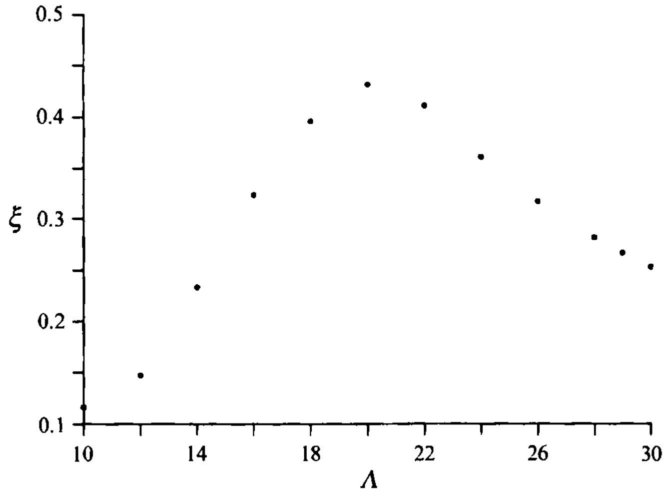

FIGURE 13. ξ plotted as a function of A.

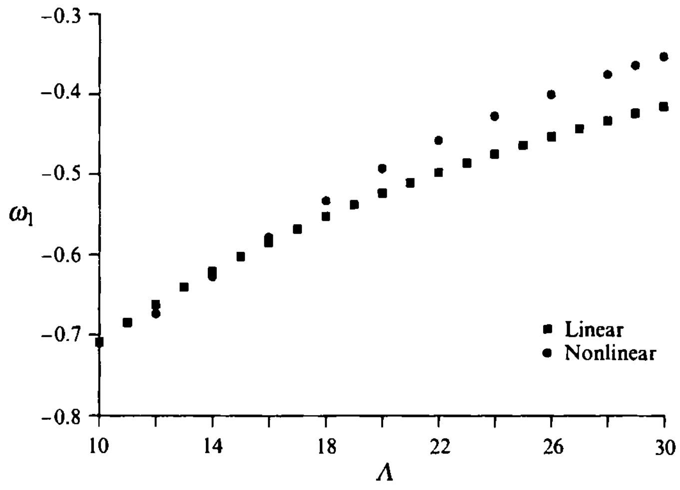

FIGURE 14. Frequency of the $(m = 1, n = 1)$ mode, ω_1 plotted as a function of A. Solid circles represent the frequency found from the nonlinear calculation and solid boxes represent the frequency found from the linear calculation.

There are, of course, a number of further steps that need to be made. Perhaps the most fundamental step is an examination of more realistic ϵ, i.e. we need to lower ϵ substantially. As discussed in §4 the current choice of ϵ is numerically expedient, but not necessarily representative of the Earth's core and it would be imprudent to make comparisons between the flows found here and those found from observation. Of course the most undesirable effect of lowering ϵ will be the need to increase the number of spectral functions, which in turn means that we will need to reduce the timestep to satisfy the Courant condition. One of our early presumptions was that we would be able to restrict the truncation in the axial and azimuthal directions to a few modes: the linear theory predicts that for a choice of A just greater than A_c for the most unstable mode, higher wavenumber modes will simply decay. However in the nonlinear case the most unstable mode grows and transfers energy to the higher wavenumber modes so that it is no longer valid to truncate the expansions at low angular order – in general we required between 20 and 42 angular modes to resolve the nonlinear equilibrated solution (see table 3). The calculation of nonlinearities in ϕ and z is currently designed for low angular order, but it would be a relatively simple matter to calculate these nonlinearities using FFTs, which would speed up the calculation for higher M and N.

We also need to examine basic states that better mimic fields that may occur in the core (e.g. low-order decay modes – see Zhang & Fearn 1993) and investigate the effect the boundary conditions have on the type of solution found. Further, the instability we have investigated here is generally of resistive type. It would also be instructive to study ideal instabilities and investigate their behaviour as they evolve to finite amplitude.

This work is supported by the Particle Physics and Astronomy Research Council of Great Britain under grant GR/H 03506.

Appendix. Numerical method

In space, the governing equations are solved spectrally and each dependent variable is approximated by a finite sum of expansion functions. The stress-free, perfectly conducting flat ends enable us to choose expansion functions in z that automatically satisfy the boundary conditions (2.21)

$$\left\{\begin{array}{l} v(s,z) \\ h(s,z) \\ V(s,z) \\ H(s,z) \end{array}\right\} = \left\{\begin{array}{l} v(s) \\ h(s) \\ V(s) \\ H(s) \end{array}\right\} \sin\frac{k\pi}{2\zeta}(z+\zeta), \tag{A 1}$$

$$\left\{\begin{array}{l} w(s,z) \\ g(s,z) \\ W(s,z) \\ G(s,z) \end{array}\right\} = \left\{\begin{array}{l} w(s) \\ g(s) \\ W(s) \\ G(s) \end{array}\right\} \cos\frac{k\pi}{2\zeta}(z+\zeta). \tag{A 2}$$

These expansions have been used by Lan, Kuang & Roberts (1993). Notice that the axial wavenumber, n, of Fearn (1983) is related to the k of (A 1) and (A 2) by $n = k\pi/2\zeta$. In the radial direction we expand our dependent variables in terms of Chebychev functions $T_l\,(x)$ where s is mapped into coordinate x by

$$x = \frac{2s-1-s_{ib}}{1-s_{ib}}.$$

This mapping allows us to use the Chebychev mesh points defined by a Gauss–Lobatto grid

$$x_i = \cos(i\pi/L), \qquad i = 0, 1, \ldots, L-1, L, \tag{A 3}$$

which means that the Chebychev polynomials are just cosine functions. Notice that these mesh points include the boundaries $x = \pm 1$. In the ϕ-direction the dependent variables are expanded in terms of complex Fourier series. The eight dependent variables can therefore be expressed as

$$V(x,z,t) = \sum_{k=1}^{k=K} \sum_{l=0}^{l=L+2} \hat{V}_{lk}(t) \sin\frac{k\pi}{2\zeta}(z+\zeta)\;\; T_l\,(x), \tag{A 4}$$

$$W(x,z,t)=\sum_{k=0}^{k=K}\sum_{l=0}^{l=L}\hat{W}_{lk}(t)\cos\frac{k\pi}{2\zeta}(z+\zeta)\;T_l\,(x), \tag{A 5}$$

$$H(x,z,t)=\sum_{k=1}^{k=K}\sum_{l=0}^{l=L}\hat{H}_{lk}(t)\sin\frac{k\pi}{2\zeta}(z+\zeta)\;T_l\,(x), \tag{A 6}$$

$$G(x,z,t)=\sum_{k=0}^{k=K}\sum_{l=0}^{l=L}\hat{G}_{lk}(t)\cos\frac{k\pi}{2\zeta}(z+\zeta)\;T_l\,(x), \tag{A 7}$$

$$w(x,\phi,z,t)=\sum_{m=1}^{m=M}\sum_{k=0}^{k=K}\sum_{l=0}^{l=L+2}\hat{w}_{lkm}(t)\cos\frac{k\pi}{2\zeta}(z+\zeta)\;T_l\,(x)\mathrm{e}^{\mathrm{i}m\phi}+\text{c.c.}, \tag{A 8}$$

$$v(x,\phi,z,t)=\sum_{m=1}^{m=M}\sum_{k=1}^{k=K}\sum_{l=0}^{l=L}\hat{v}_{lkm}(t)\sin\frac{k\pi}{2\zeta}(z+\zeta)\;T_l\,(x)\mathrm{e}^{\mathrm{i}m\phi}+\text{c.c.}, \tag{A 9}$$

$$g(x,\phi,z,t)=\sum_{m=1}^{m=M}\sum_{k=0}^{k=K}\sum_{l=0}^{l=L}\hat{g}_{lkm}(t)\cos\frac{k\pi}{2\zeta}(z+\zeta)\;T_l\,(x)\mathrm{e}^{\mathrm{i}m\phi}+\text{c.c.}, \tag{A 10}$$

$$h(x,\phi,z,t)=\sum_{m=1}^{m=M}\sum_{k=1}^{k=K}\sum_{l=0}^{l=L}\hat{h}_{lkm}(t)\sin\frac{k\pi}{2\zeta}(z+\zeta)\;T_l\,(x)\mathrm{e}^{\mathrm{i}m\phi}+\text{c.c.} \tag{A 11}$$

Notice that we have included two extra terms in the radial spectral sum for w and V – this ensures that the resulting equations and boundary conditions form a complete set – there are four boundary conditions for each of w and V.

Our numerical method closely follows the methods described in Jones (1981, 1985), Barenghi & Jones (1989) and Barenghi (1991). To illustrate the method we shall describe the axisymmetric expansion (the non-axisymmetric variables are treated similarly). Axisymmetric expansions (A 4)–(A 7) give us a set of $(4K+2)(L+1)+2K$ unknown coefficients in time. Substituting these expansions into the boundary conditions (2.21) and (2.22) gives $10K+4$ equations – we therefore need a further $(4K+2)(L-1)$ equations for closure. We retrieve the first set of equations by a Galerkin method in the z-direction: we substitute our expansions into the governing equations (2.13)–(2.16), multiply each equation by a test function (either $\cos p\pi(z+\zeta)/2\zeta$ or $\sin p\pi(z+\zeta)/2\zeta$) and then integrate over the cylinder height. For example, to retrieve a Galerkin equation for H (the axisymmetric vector potential) we substitute our expansions into (2.16) and multiply the resulting equation by $\sin p\pi(z+\zeta)/2\zeta$ and integrate from $-\zeta$ to $+\zeta$. The nonlinear terms that contain products of sines and products of cosines are then expressed as the sums of cosines. A similar process is carried out for the other equations, resulting in a total of $4K+2$ Galerkin equations. In the radial direction collocation is used, whereby the test functions are shifted Dirac delta-functions centred on so-called collocation points (A 3), and we demand that each equation must be satisfied at each of the $(L-1)$ interior collocation points. Boundary conditions are explicitly imposed at x_0 and x_L. The Galerkin-collocation method gives the extra $(4K+2)(L-1)$ equations required.

For the non-axisymmetric variables we carry out the same process, but we also use a Galerkin method the azimuthal direction. For example, given the non-axisymmetric momentum equations

$$\bar{\boldsymbol{A}}\boldsymbol{u} = \boldsymbol{v}$$

where $\bar{\boldsymbol{A}}$ is a matrix of linear operators and boundary conditions, $\boldsymbol{u}$ is the non-axisymmetric solution vector and $\boldsymbol{v}$ is the nonlinear Lorentz vector, our Galerkin-collocation method leads to the following matrix-vector structure:

$$\begin{bmatrix} \boxed{\bar{\mathbf{C}}_{10}} & & & & & & & \\ & \boxed{\bar{\mathbf{C}}_{11}} & & & & & & \\ & & \ddots & & & & & \\ & & & \boxed{\bar{\mathbf{C}}_{1K}} & & & & \\ & & & & \ddots & & & \\ & & & & & \boxed{\bar{\mathbf{C}}_{M0}} & & \\ & & & & & & \boxed{\bar{\mathbf{C}}_{M1}} & \\ & & & & & & & \ddots \\ & & & & & & & & \boxed{\bar{\mathbf{C}}_{MK}} \end{bmatrix} \begin{bmatrix} u_{10} \\ u_{11} \\ \vdots \\ u_{1K} \\ \vdots \\ u_{M0} \\ u_{M1} \\ \vdots \\ u_{MK} \end{bmatrix} = \begin{bmatrix} v_{10} \\ v_{11} \\ \vdots \\ v_{1K} \\ \vdots \\ v_{M0} \\ v_{M1} \\ \vdots \\ v_{MK} \end{bmatrix}$$

Matrix $\bar{\boldsymbol{A}}$ is a 'diagonal' matrix with 'elements' which are, in turn, collocation matrices: i.e. for each (m, k) Galerkin combination there is a corresponding collocation matrix $\bar{\mathbf{C}}_{mk}$.

The time integration of the induction equation is performed in mixed physical–spectral space (x, m, k). We apply an unconditionally stable method for the linear diffusion terms – the Crank–Nicolson (CN) method – and we use an explicit Adams–Bashforth (AB) method for the remaining nonlinear terms. If for axial wavenumber k, we write the H-equation (2.16) at collocation point x_i as

$$\frac{\partial \hat{H}_{ik}(x_i, t)}{\partial t} = \mathit{\Lambda}^{-1}\mathrm{D}^2\hat{H}_{in}(x_i, t) + \hat{F}_{ik}(x_i, t),$$

where $\hat{F}_{ik}$ is a typical nonlinear coefficient of $[\nabla\times(\boldsymbol{U} \times \boldsymbol{B})]_\phi$ at point x_i,then in our CN–AB representation

$$\frac{\hat{H}_{ik}(x_i, t + \Delta t) - \hat{H}_{ik}(x_i, t)}{\Delta t} = \\ \mathit{\Lambda}^{-1}/2[D^2(\hat{H}_{ik}(x_i, t + \Delta t)) + D^2(\hat{H}_{ik}(x_i, t))] + \tfrac{1}{2}[3\hat{F}_{ik}(x_i, t) - \hat{F}_{ik}(x_i, t - \Delta t)].$$

Since the CN method is implicit, the dependent variable at the new timestep (in this case $\hat{H}_{ik}(x_i, t + \Delta t)$) appears on both sides of the equation. Because of this we need to invert a matrix but this need only be carried out once and then stored for future time integrations. Given the total magnetic and velocity fields at timesteps t and $t - \Delta t$, we can advance the total magnetic field to timestep $t + \Delta t$. Subsequently the diagnostic momentum equations are solved at timestep $t + \Delta t$.

Because the dependent variables have been expanded in terms of well-known functions it is easy to differentiate accurately in spectral space. For the Chebychev functions differentiation is carried out using recursion relations, whilst Fourier differentiation is carried out directly (i.e. by multiplying by powers of the axial or azimuthal wavenumbers as appropriate). In the radial direction fast Fourier transforms (FFTs) are used to move between physical space (x) and spectral space (l) – multiplications are performed at collocation points x_i. (Aliasing errors are spectrally small and can be neglected.) In the angular directions multiplications are carried out in spectral space where products of cosines and sines are expressed as sums of cosines and sines etc. These nonlinear algorithms were checked against test data, whereby two vectors $f(s,\phi,z,t)$ and $g(s,\phi,z,t)$ were used as input, their nonlinear products calculated analytically, and compared with results from the nonlinear code.

REFERENCES

ACHESON, D. J. 1972 On the hydromagnetic stability of a rotating fluid annulus. *J. Fluid Mech.* **52**, 529–541.

ACHESON, D. J. 1973 Hydromagnetic wave-like instabilities in a rapidly rotating stratified fluid. *J. Fluid Mech.* **61**, 609–624.

ACHESON, D. J. 1978 Magnetohydrodynamic waves and instabilities in rotating fluids. In *Rotating Fluids in Geophysics* (ed. P. H. Roberts & A. M. Soward), pp. 315–349. Academic Press.

ACHESON, D. J. 1983 Local analysis of thermal and magnetic instabilities in a rapidly rotating fluid. *Geophys. Astrophys. Fluid Dyn.* **27**, 123–136.

BARENGHI, C. F. 1991 Computations of transitions and Taylor vortices in temporally modulated Taylor-Couette flow. *J. Comput. Phys.* **95**, 175–194.

BARENGHI, C. F. & JONES, C. A. 1989 Modulated Taylor-Couette flow. *J. Fluid Mech.* **208**, 127–160.

BLOXHAM, J., GUBBINS, D. & JACKSON, A. 1989 Geomagnetic secular variation. *Phil. Trans. R. Soc. Lond.* **329**, 415–502.

FEARN, D. R. 1983 Hydromagnetic waves in a differentially rotating annulus I. A test of local stability analysis. *Geophys. Astrophys. Fluid Dyn.* **27**, 137–162.

FEARN, D. R. 1984 Hydromagnetic waves in a differentially rotating annulus II. Resistive instabilities. *Geophys. Astrophys. Fluid Dyn.* **30**, 227–239.

FEARN, D. R. 1985 Hydromagnetic waves in a differentially rotating annulus III. The effect of an axial field. *Geophys. Astrophys. Fluid Dyn.* **33**, 185–197.

FEARN, D. R. 1988 Hydromagnetic waves in a differentially rotating annulus IV. Insulating boundaries. *Geophys. Astrophys. Fluid Dyn.* **44**, 55–75.

FEARN, D. R. 1989 Differential rotation and thermal convection in a rapidly rotating hydromagnetic system. *Geophys. Astrophys. Fluid Dyn.* **44**, 55–75.

FEARN, D. R. & WEIGLHOFER, W. S. 1991*a* Magnetic instabilities in rapidly rotating spherical geometries I. From cylinders to spheres. *Geophys. Astrophys. Fluid Dyn.* **56**, 159–181.

FEARN, D. R. & WEIGLHOFER, W. S. 1991*b* Magnetic instabilities in rapidly rotating spherical geometries II. More realistic fields and resistive instabilities. *Geophys. Astrophys. Fluid Dyn.* **60**, 275–294.

FEARN, D. R. & WEIGLHOFER, W. S. 1992*a* Resistive instability and the magnetostrophic approximation. *Geophys. Astrophys. Fluid Dyn.* **63**, 111–138.

FEARN, D. R. & WEIGLHOFER, W. S. 1992b Magnetic instabilities in rapidly rotating spherical geometries III. The effect of differential rotation. *Geophys. Astrophys. Fluid Dyn.* **67**, 163–185.

GUBBINS, D. & ROBERTS P. H. 1987 Magnetohydrodynamics of the earth's core. In *Geomagnetism* (ed. J. A. Jacobs), Vol. 2, pp. 1–183. Academic Press.

HOLLERBACH, R. & IERLEY, G. I. 1991 A modal α^2-dynamo in the limit of asymptotically small viscosity. *Geophys. Astrophys. Fluid Dyn.* **56**, 133–158.

IERLEY, G. I. 1985 Macrodynamics of α^2 dynamos. *Geophys. Astrophys. Fluid Dyn.* **34**, 143–173.

JONES, C. A. 1981 Nonlinear Taylor vortices and their stability. *J. Fluid Mech.* **102**, 249–261.

JONES, C. A. 1985 Numerical methods for the transition to wavy Taylor vortices. *J. Comput. Phys.* **61**, 321–344.

LAN, S., KUANG, W. & ROBERTS, P. H. 1993 Ideal instabilities in rapidly rotating MHD systems that have critical layers. *Geophys. Astrophys. Fluid Dyn.* **69**, 133–160.

KNOBLOCH, E. 1994 Bifurcations in rotating systems. In *Lectures on Solar and Planetary Dynamos* (ed. M. R. E. Proctor & A. D. Gilbert). Cambridge University Press.

MCFADDEN, P. L. & MERRILL, R. T. 1993 Inhibition and geomagnetic reversals. *J. Geophys. Res.* **98**, 6189–6199.

TAYLOR, J. B. 1963 The magneto-hydrodynamics of a rotating fluid and the Earth's dynamo problem. *Proc. R. Soc. Lond.* A **274**, 274–283.

ZHANG, K. & FEARN, D. R. 1993 How strong is the invisible component of the magnetic field in the earth's core. *Geophys. Res. Lett.* **20**, 2083–2086.

ZHANG, K. & FEARN, D. R. 1994 Hydromagnetic waves in rapidly rotating spherical shells, generated by magnetic toroidal decay modes. *Geophys. Astrophys. Fluid Dyn.* **77**, 123–147.